



Z-scheme plasmonic Ag decorated $\text{WO}_3/\text{Bi}_2\text{WO}_6$ hybrids for enhanced photocatalytic abatement of chlorinated-VOCs under solar light irradiation

Hongru Zhou^a, Zhipan Wen^a, Jie Liu^b, Jun Ke^{a,*}, Xiaoguang Duan^c, Shaobin Wang^{c,*}



^a School of Chemistry and Environmental Engineering, Wuhan Institute of Technology, Wuhan, 430205, China

^b Department of Environmental Science & Engineering, North China Electric Power University, Baoding, 071003, China

^c School of Chemical Engineering, the University of Adelaide, Adelaide, SA, 5005, Australia

ARTICLE INFO

Keywords:

Photocatalysis
Volatile organic compounds
Z-scheme
Plasmonic Ag
 $\text{WO}_3/\text{Bi}_2\text{WO}_6$ heterojunction

ABSTRACT

Ag decorated $\text{WO}_3/\text{Bi}_2\text{WO}_6$ hybrid heterojunction with a direct Z-scheme band structure has been synthesized by a novel method for efficient removal of gaseous chlorinated-volatile organic compounds (VOCs) under simulated sunlight irradiation. Bismuth atoms were inserted into the $[\text{WO}_6]$ layers of tungstate acid to form $[\text{Bi}_2\text{O}_2]$ layers toward the formation of a Bi_2WO_6 crystal phase, which results in Z-scheme $\text{WO}_3/\text{Bi}_2\text{WO}_6$ heterojunction. Ag nanoparticles (NPs) were further introduced and uniformly anchored on the surface of the $\text{WO}_3/\text{Bi}_2\text{WO}_6$ for improving visible-light absorption and adjusting behavior of photoinduced charge carriers in the heterostructure through surface plasmon resonance (SPR). In comparison with pristine Bi_2WO_6 and $\text{WO}_3/\text{Bi}_2\text{WO}_6$, Ag/ $\text{WO}_3/\text{Bi}_2\text{WO}_6$ exhibits a better photocatalytic activity for removal of gaseous chlorobenzene under simulated sunlight irradiation. The conversion efficiency of 2% Ag/ $\text{WO}_3/\text{Bi}_2\text{WO}_6$ heterojunction is 2.5 and 1.9 times higher than those of the pristine Bi_2WO_6 and $\text{WO}_3/\text{Bi}_2\text{WO}_6$ samples, respectively. The improved photocatalytic activity is mainly attributed to the formation of three-component heterojunction with the Z-scheme structure and SPR effect of Ag NPs, which could not only increase absorption of visible light, but also promote the separation efficiency of photogenerated electrons and holes in the hybrids.

1. Introduction

From the viewpoint of sustainable development, heterogeneous photocatalysis by utilizing solar energy for environmental remediation and water splitting is a promising approach to solve the increasing environmental issue and energy crisis. In general, the heterogeneous photocatalysis could involve in three steps, where photons are firstly harvested to produce electron-hole pairs on the surface and shallow atom layers of a solid photocatalyst [1,2]. Subsequently, the photo-generated charge carriers transport to the surface of the solid photocatalyst and react with H_2O or O_2 to produce reactive oxygen species (ROS), such as $\cdot\text{OH}$ and $\cdot\text{O}_2^-$ [3,4]. Finally, the adsorbed target substances, such as CO_2 , volatile organic compounds (VOCs) and water, are oxidized or reduced by the ROS and electrons [5–7]. For example, TiO_2 -based photocatalysts were reported for degradation of gaseous chlorobenzene under UV irradiation [8,9]. In addition, some groups studied the photocatalytic oxidation of monochlorobenzene over photocatalysts in aqueous phase, exhibiting great photocatalytic activities [10]. Therefore, the vital issue of this photocatalytic process is the development of novel photocatalysts with efficient separation, electron transfer

and utilization of photoinduced charge carriers for excellent photocatalytic performance.

To achieve a better photocatalytic activity, intensive researches have been focused on developing novel ternary metal oxides as efficient photocatalysts, such as ZnFe_2O_4 [11], Bi_2MoO_6 [12,13], and CuWO_4 [14,15], due to their more flexible compositions and unique electronic structure. As a layered Aurivillius-related oxide semiconductor, bismuth tungstate (Bi_2WO_6) is composed of alternating corner-sharing $[\text{WO}_6]$ octahedral layers and $[\text{Bi}_2\text{O}_2]$ layers and is a promising photosensitive material due to its optical properties, for example, a suitable band gap of 2.75 eV and good photostability [16–18]. Moreover, density functional theory (DFT) calculation shows that the conduction band (CB) of Bi_2WO_6 is comprised of W 5d orbitals; whereas its valence band (VB) is mainly formed by hybridization of O 2p with Bi 6s orbitals, which not only makes the VB largely dispersed, but also favors the mobility of photo-induced holes for specific oxidation reaction [19]. However, the photocatalytic activity of Bi_2WO_6 is still limited by a poor separation efficiency of the photoinduced charge carriers in the photocatalytic reactions. Many approaches, such as constructing heterojunction [20,21], doping [22] and loading noble metals [23], have been

* Corresponding authors.

E-mail addresses: jke@wit.edu.cn (J. Ke), shaobin.wang@adelaide.edu.au (S. Wang).

explored in the past decades. Therefore, coupling Bi_2WO_6 with other semiconductors for constructing a heterojunction system can be used to improve the photocatalytic performance of Bi_2WO_6 . Among numerous semiconductors, tungsten trioxide (WO_3) possesses a suitable band gap (~ 2.7 eV) and high valence band position (+ 3.4 eV vs. NHE) [24]. In fact, WO_3 is often used as an effective photocatalyst in photocatalytic or electrocatalytic oxygen evolution reaction due to its high valence band position and strong photostability [25,26], which may be a good candidate for improving charge carrier transportation by constructing a Z-scheme system with the ternary Bi_2WO_6 according to the principles of a direct Z-scheme photocatalytic system [27,28]. In general, a Z-scheme photocatalyst simultaneously has the strong redox ability for driving photocatalytic reactions and the spatially separated reductive and oxidative active sites [29]. Furthermore, it is revealed that noble metal nanoparticles (NPs) with a surface plasmon resonance (SPR) effect and strong interaction between the noble metal and semiconductor could remarkably enhance visible light absorption and inhibit the recombination of photo-generated electrons and holes [30,31].

Based on the above strategies, in this work, three-component $\text{Ag}/\text{WO}_3/\text{Bi}_2\text{WO}_6$ heterojunction with a SPR effect was synthesized by a special route for enhanced photocatalytic decontamination of monochlorobenzene (Cl-VOCS) under simulated sunlight irradiation. Firstly, two-component heterojunction between WO_3 and Bi_2WO_6 was constructed to form a Z-scheme band structure, which could be beneficial for improving separation efficiency of photoinduced electrons and holes. Secondly, Ag NPs were introduced to harvest low energetic photons in the range of visible light due to the SPR effect. As a result, the three-component $\text{Ag}/\text{WO}_3/\text{Bi}_2\text{WO}_6$ hybrids exhibit significantly enhanced visible light response and photocatalytic performance in comparison with pristine Bi_2WO_6 and two-component $\text{WO}_3/\text{Bi}_2\text{WO}_6$, which is ascribed to the more efficient separation of photoinduced electron-hole pairs and SPR effect. In addition, the process of the photocatalytic degradation of chlorobenzene was monitored by *in-situ* FTIR and the possible reaction pathways are further discussed.

2. Experimental

2.1. Preparation of flower-like $\text{WO}_3/\text{Bi}_2\text{WO}_6$ nanostructures

$\text{WO}_3/\text{Bi}_2\text{WO}_6$ hybrids were synthesized by an ion insertion and condensation process in aqueous solution at elevated temperature. In a typical case, a bismuth stock solution with a concentration of 0.2 M was prepared by dissolution of $\text{Bi}(\text{NO}_3)_3 \cdot 5\text{H}_2\text{O}$ in 1.5 M nitric acid solution, and then the tungstate solution was obtained by dissolution of H_2WO_4 in 1.5 M nitric acid solution. The bismuth and tungstate stock solutions were mixed at a molar ratio of Bi/W = 2. The mixed solution was stirred for 30 min, and then transferred into a 100 mL Teflon-lined autoclave and maintained at 200 °C for 24 h. After that, the autoclave was naturally cooled down to room temperature and a light-yellow precipitate was collected and washed several times by deionized water and absolute ethanol. Finally, the collected precipitate was dried under nitrogen for further use.

For comparison, pristine flower-like Bi_2WO_6 and WO_3 nanoplates were prepared by using previously reported methods [17,32].

2.2. Synthesis of $\text{Ag}/\text{WO}_3/\text{Bi}_2\text{WO}_6$ hybrids

The three-component $\text{Ag}/\text{WO}_3/\text{Bi}_2\text{WO}_6$ heterojunction was prepared through a UV-assisted reduction deposition route. Firstly, different amounts of AgNO_3 and 0.5 g of the as-obtained $\text{WO}_3/\text{Bi}_2\text{WO}_6$ heterojunctions (the mass loadings of Ag to $\text{WO}_3/\text{Bi}_2\text{WO}_6$ are at 0.5% and 2%) were dissolved into 25 mL of purified water, respectively. Then an AgNO_3 solution was added into the $\text{WO}_3/\text{Bi}_2\text{WO}_6$ suspension drop by drop and stirred for 30 min in dark. UV light ($\lambda < 265$ nm) was enlightened for 5 h and the light-yellow suspension gradually became brown with the increasing of irradiation time due to photoreduction of

Ag^+ ions to metallic Ag nanoparticles. Finally, the precipitate was collected and washed by deionized water and absolute ethanol.

2.3. Characterizations

The crystal phase of the synthesized samples was measured by X-ray diffraction (XRD) using a Bruker axs D8 Discover system operated at 40 kV and 40 mA with $\text{Cu-K}\alpha$ radiation ($\lambda = 1.5418 \text{ \AA}$) at a scan rate of 5°/min. Transmission electron microscopy (TEM) was operated at 200 kV on JEOL JEM2100. High resolution transmission electron microscopy (HRTEM) was taken on TITAN. Raman spectra of the samples were recorded by ISA dispersive Raman spectroscopy using argon ion laser with 633 nm excitation. Fourier transform infrared measurements (FTIR) were recorded on KBr pellets with a Bruker Tensor 27. Diffuse reflectance electronic spectra (DRS) were measured by a Hitachi UH 4150 equipped with an integrating sphere accessory. X-ray photoelectron spectroscopy (XPS) and valence band XPS (VB-XPS) of various samples were tested on a Kratos AXIS Ultra DLD system under ultrahigh vacuum (UHV) conditions, and the binding energies of C 1 s, Bi 4f, W 4f and O 1 s were calibrated using C 1 s (BE = 284.8 eV) as a standard. In addition, solid-state electron spin resonance (ESR) tests at low temperature were conducted at $T = -196$ °C. The settings for the ESR spectrometer were as follows: center field = 3420 G; sweep width = 200 G; microwave frequency = 9.85 GHz; modulation frequency = 100 kHz and power = 10 mW.

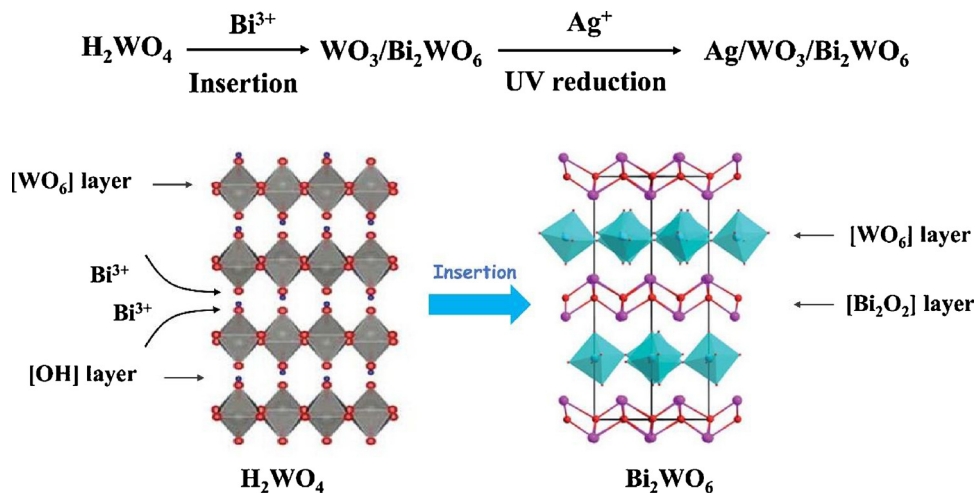
2.4. Evaluation of photocatalytic activity

Photocatalytic activities of the catalysts were measured using photocatalytic conversion of chlorobenzene under simulated sunlight irradiation in a 120 mL homebuilt quartz photoreaction cell equipped with two KBr windows and a sample holder (diameter, 13 mm) for the catalyst wafer (0.2 g). After the catalyst was placed in the sample holder, 2 μL of chlorobenzene was injected into the reactor with a microsyringe, mixed with air at the relative humidity of 45% and the reaction temperature of ~ 25 °C. When the photocatalyst sample reached adsorption equilibrium in the reactor for 1 h, a Xenon lamp (300 W) was turned on. The IR spectra were continuously collected on the Bruker Tensor 27 with a resolution of 1 cm^{-1} and 32 scans in the region of 4000–400 cm^{-1} during the photocatalytic reaction. The concentrations of chlorobenzene were analyzed by a gas chromatograph (Agilent 7890 A) equipped with FID (HP-5 capillary column, $30 \text{ m} \times 0.32 \text{ mm} \times 1 \mu\text{m}$).

3. Results and discussion

3.1. Structure and morphology of the synthesized $\text{Ag}/\text{WO}_3/\text{Bi}_2\text{WO}_6$ compositions

The two-component $\text{WO}_3/\text{Bi}_2\text{WO}_6$ heterojunction was fabricated through a one-pot route using tungstate acid as a starting material (Scheme 1). The introduced Bi^{3+} ions from $\text{Bi}(\text{NO}_3)_3$ in strong acidic condition could react with tungstate acid, where the Bi atoms could be inserted into the $[\text{WO}_6]$ layers to form $[\text{Bi}_2\text{O}_2]$ layers under certain temperature and pressure, which is consisting of Bi_2WO_6 crystal phase. At the late stage of the reaction under certain temperature, the insertion reaction of Bi^{3+} was very slow due to the low concentration of Bi^{3+} in the solution, which resulted in the dehydration of H_2WO_4 to form WO_3 crystal phase. After that, Ag NPs are deposited on the surface of the two-component $\text{WO}_3/\text{Bi}_2\text{WO}_6$ through a benign UV-assisted photoreduction route, which is beneficial for a uniform distribution of Ag NPs. The crystal structure of the as-synthesized sample was measured and displayed in Fig. 1a. It is observed that the samples synthesized at 160, 180, and 200 °C possess two independent crystal phases attributed to russellite Bi_2WO_6 (PDF#39-0256) and monoclinic WO_3 (PDF#32-1395), which indicates that the reaction between Bi^{3+} and tungstate is



Scheme 1. Illustrator of the synthetic process of the three-component $\text{Ag}/\text{VO}_3/\text{Bi}_2\text{WO}_6$.

insufficient despite the addition of stoichiometric starting materials [33,34]. Meanwhile, it is found that the peak intensity of VO_3 is gradually decreased at elevated reaction temperature, which suggests that high reaction temperature could consolidate the occupation of Bi ions in H_2WO_4 and facilitate the formation of Bi_2WO_6 crystal phase, thus decreasing the proportion of VO_3 from condensation of the unreacted H_2WO_4 . For the prepared $\text{Ag}/\text{VO}_3/\text{Bi}_2\text{WO}_6$ hybrids, although the diffraction patterns are similar to the $\text{VO}_3/\text{Bi}_2\text{WO}_6$ heterojunctions, the peak at 38.2° attributed to metallic Ag (111) facet is detected, which indicates that the introduced Ag^+ ions were successfully reduced to metallic Ag under UV light irradiation [35].

Raman spectra of the prepared samples were recorded to further confirm the formation of the three-component heterojunctions. As depicted in Fig. 1b, the bands at 796 and 828 cm^{-1} are assigned to the antisymmetric and symmetric A_g modes of terminal O–W–O, respectively. The medium peak centered at 710 cm^{-1} is attributed to the asymmetric stretching vibration between the W plane and O atoms [36]. The strong peak centered at 306 cm^{-1} and shoulders are mainly due to the stretching or bending vibrations of the VO_6 octahedron, BiO_6 polyhedron, and Bi–O bonds [37,38]. When $\text{VO}_3/\text{Bi}_2\text{WO}_6$ heterojunction is formed, these characteristic peaks are still observed except for the peak at 828 cm^{-1} , which is weakened significantly. We speculate that the surficial interaction between VO_3 and Bi_2WO_6 interfere the symmetric vibration of O–W–O in Bi_2WO_6 crystal structure, resulting in the weaker peak intensity. In contrast, the antisymmetric vibration of A_g modes is increased apparently, which further testifies the formation of the heterojunction between VO_3 and Bi_2WO_6 . After deposition of Ag NPs on the surface of $\text{VO}_3/\text{Bi}_2\text{WO}_6$, the Raman spectra

remain unchanged except for appearance of a shoulder peak at 886 cm^{-1} , which is assigned to the shortest Raman fingerprint of W–O bond ($\nu\text{s}(\text{W}=\text{O})$) [39]. This may indicate that Ag NPs are deposited on the surface of Bi_2WO_6 .

The general morphologies of $\text{VO}_3/\text{Bi}_2\text{WO}_6$ and $\text{Ag}/\text{VO}_3/\text{Bi}_2\text{WO}_6$ samples were presented in Fig. 2a and b. In the case of the two-component $\text{VO}_3/\text{Bi}_2\text{WO}_6$ heterojunctions, a flower-like hierarchical structure is formed, consisting of nanosheets with thickness of approximately 12 nm , as shown in Fig. 2b and Fig. S1.

Furthermore, the EDX spectrum of the two-component $\text{VO}_3/\text{Bi}_2\text{WO}_6$ sample indicates that the main elements are Bi, W, and O (inset of Fig. 2a). After Ag was loaded on the surface of $\text{VO}_3/\text{Bi}_2\text{WO}_6$, it is found that the surface of hierarchical structure became smoother in comparison with the unloaded sample, as shown in Fig. 2c and d, which mainly results from mechanical friction, leading to loss of fine nanosstructure. Although the nanosized Ag nanoparticles are not observed on the surface of the three-component hybrids, the EDX spectrum demonstrates the existence of Ag element, as presented in the inset of Fig. 2c.

Furthermore, the morphologies of $\text{VO}_3/\text{Bi}_2\text{WO}_6$ and $\text{Ag}/\text{VO}_3/\text{Bi}_2\text{WO}_6$ samples were revealed by TEM and HRTEM images. In Fig. 3a, the nanosheets from the hierarchical $\text{VO}_3/\text{Bi}_2\text{WO}_6$ sample are displayed because of sonication effect, which demonstrates that the sheets possess an ultrathin structure and could provide more reaction sites on the surface of the nanosheets. The HRTEM image displays that two different lattice fringes are detected in Fig. 3b, where 0.32 nm and 0.37 nm of d spacing are attributed to the Bi_2WO_6 (131) facet and VO_3 (020) facet, respectively [40,41]. In case of three-component $\text{Ag}/\text{VO}_3/\text{Bi}_2\text{WO}_6$,

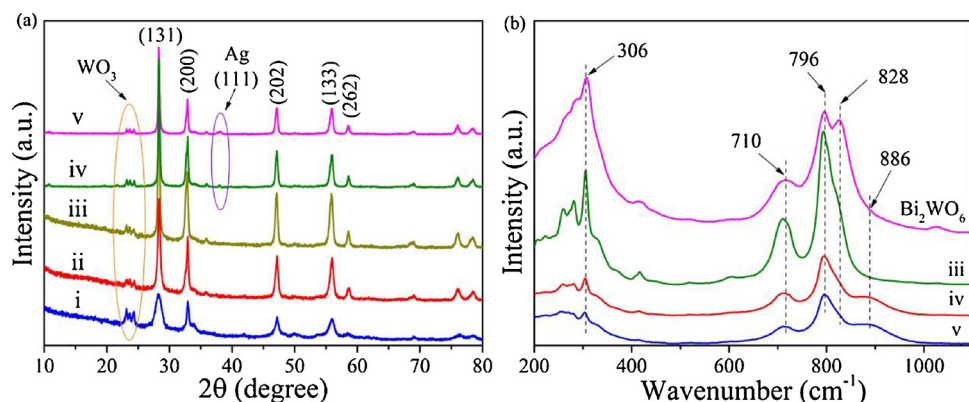


Fig. 1. XRD patterns (a) and Raman spectra (b) of the prepared samples: (i) $\text{VO}_3/\text{Bi}_2\text{WO}_6$ -160, (ii) $\text{VO}_3/\text{Bi}_2\text{WO}_6$ -180, (iii) $\text{VO}_3/\text{Bi}_2\text{WO}_6$ -200, (iv) 0.5% $\text{Ag}/\text{VO}_3/\text{Bi}_2\text{WO}_6$, (v) 2% $\text{Ag}/\text{VO}_3/\text{Bi}_2\text{WO}_6$.

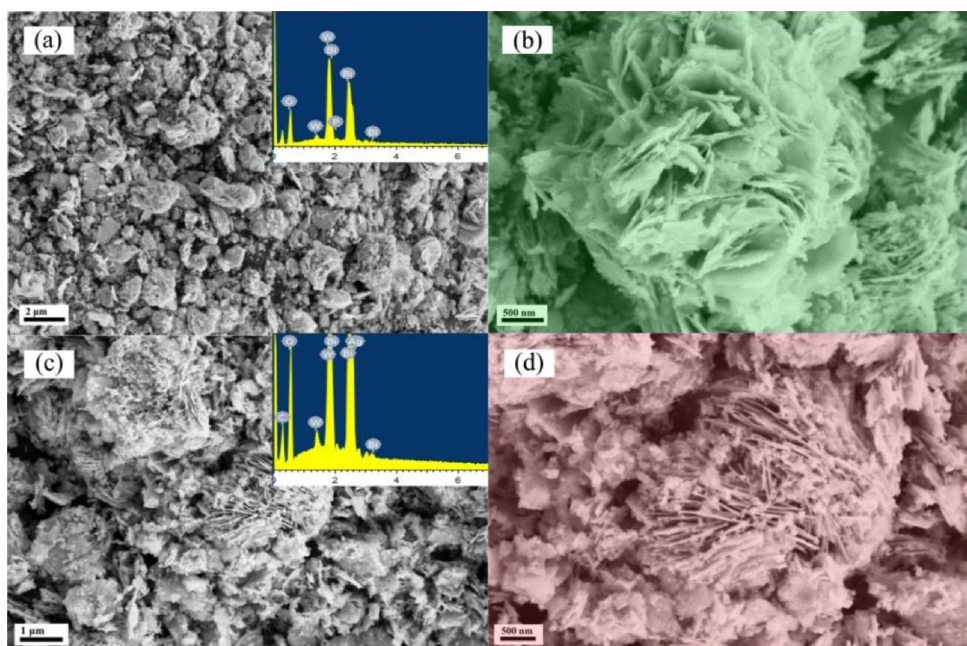


Fig. 2. SEM images of the WO₃/Bi₂WO₆ (a, b) and 2% Ag/WO₃/Bi₂WO₆ (c, d). The inset pictures are corresponding results of energy dispersive X-ray spectroscopy (EDX).

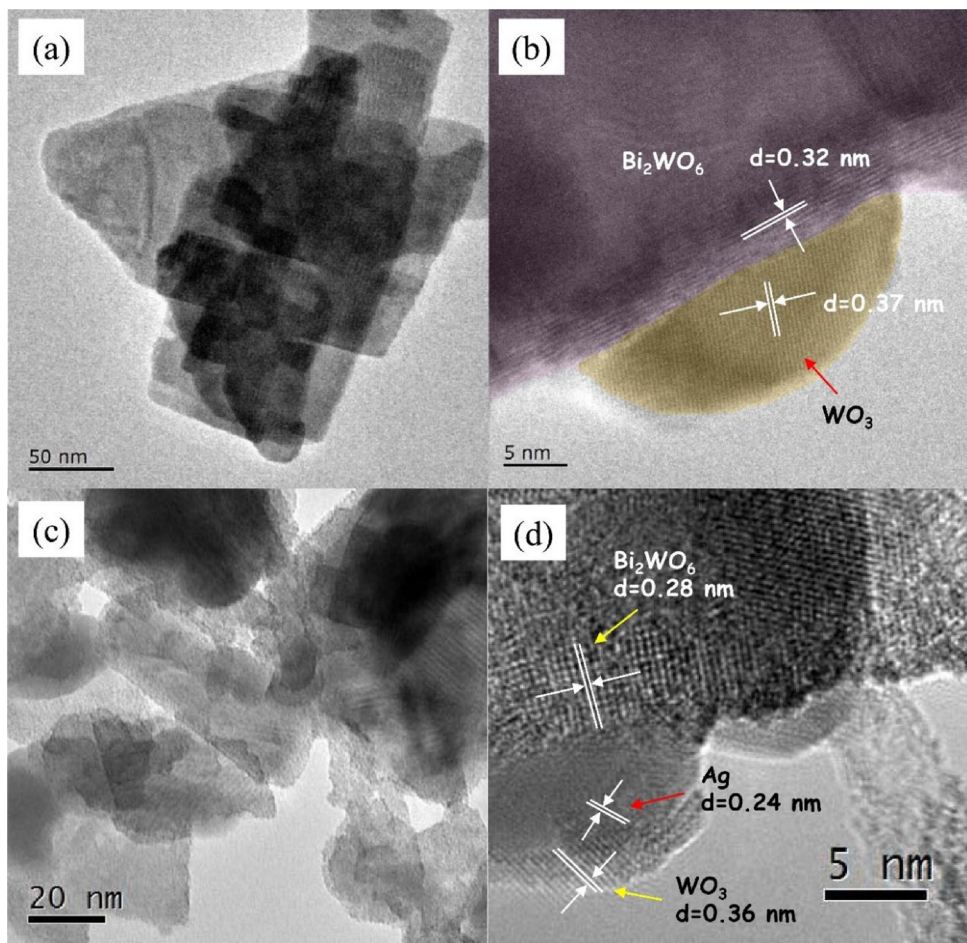


Fig. 3. TEM and HRTEM images of the prepared WO₃/Bi₂WO₆ (a, b) and 2%wt Ag/WO₃/Bi₂WO₆ (c, d) hybrids.

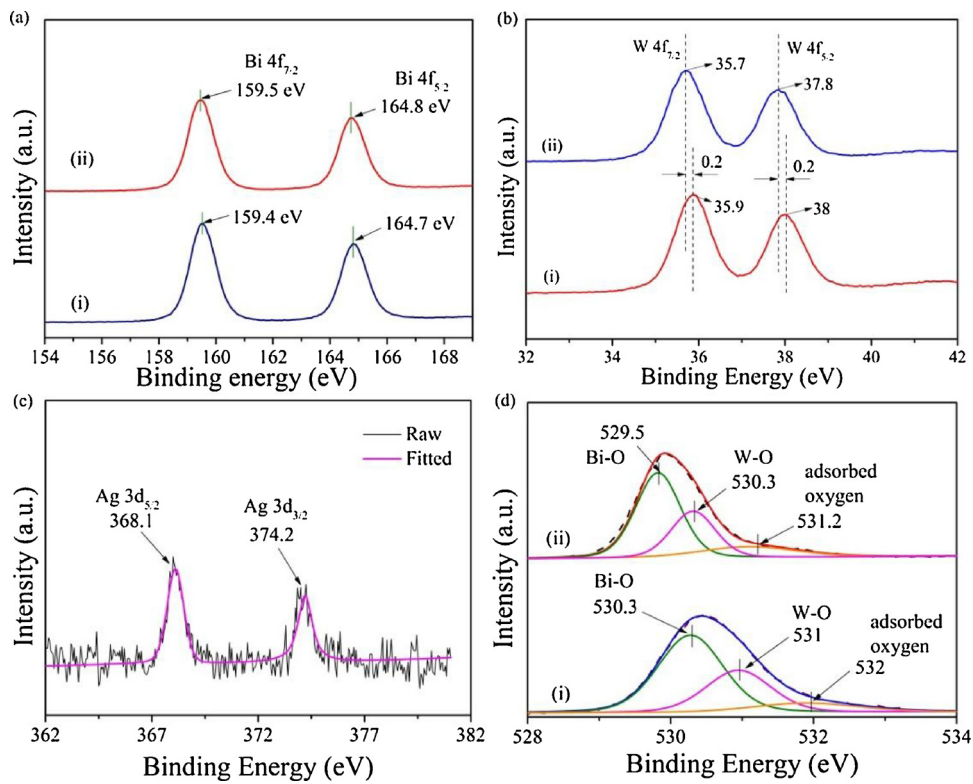


Fig. 4. XPS spectra of Bi4f (a), W4f (b), Ag3d (c), and O1 s (d) of the prepared $\text{WO}_3/\text{Bi}_2\text{WO}_6$ (i) and 2% Ag/ $\text{WO}_3/\text{Bi}_2\text{WO}_6$ (ii) samples.

Bi_2WO_6 sample, the sheet-like morphology is still observed, as shown in Fig. 3c, which indicates that the strong irradiation of UV light has a negligible influence on the morphology of the $\text{WO}_3/\text{Bi}_2\text{WO}_6$ sample. The HRTEM of the Ag/ $\text{WO}_3/\text{Bi}_2\text{WO}_6$ sample displays three apparent lattice fringes, where the 0.28, 0.36, and 0.24 nm are attributed to the Bi_2WO_6 (200) facet, WO_3 (200) facet, and Ag (111) facet, respectively [42,43]. This demonstrates the co-existence of WO_3 , Bi_2WO_6 , and Ag in the sample. Moreover, it was found that some atomic defects are formed after the deposition of Ag NPs due to the strong UV light irradiation, which is beneficial for providing more active sites on the surface of the heterojunctions [44].

For the chemical states of the prepared $\text{WO}_3/\text{Bi}_2\text{WO}_6$ and Ag/ $\text{WO}_3/\text{Bi}_2\text{WO}_6$ samples, X-ray photoelectron spectroscopy (XPS) was used (Fig. 4). The survey spectra of $\text{WO}_3/\text{Bi}_2\text{WO}_6$ and 2% Ag/ $\text{WO}_3/\text{Bi}_2\text{WO}_6$ identify Bi, W, and O elements (Fig. S2). Meanwhile, Ag elements are found, revealing successful introduction to $\text{WO}_3/\text{Bi}_2\text{WO}_6$ through the UV light photo-reduction process. The corresponding XPS spectra of Bi4f, W4f, O1 s and Ag3d are presented in Fig. 4b-d. For $\text{WO}_3/\text{Bi}_2\text{WO}_6$, the characteristic spin orbit peaks at around 164.7 and 159.4 eV are ascribed to Bi 4f_{5/2} and Bi 4f_{7/2} from Bi³⁺ in the lattice of Bi_2WO_6 and the peaks at 38 and 35.9 eV are corresponded to W 4f_{5/2} and W 4f_{7/2}, respectively, which symbolized the oxidation state of W⁶⁺ [45,46]. In the case of 2% Ag/ $\text{WO}_3/\text{Bi}_2\text{WO}_6$, the binding energies of Bi 4f_{5/2} and Bi 4f_{7/2} are centered at 164.8 and 159.5 eV, respectively, which are 0.1 eV higher than those of $\text{WO}_3/\text{Bi}_2\text{WO}_6$ sample. In contrast, the peaks of W 4f_{5/2} and W 4f_{7/2} are positioned at 37.8 and 35.7 eV, respectively, decreasing by 0.2 eV as compared to the $\text{WO}_3/\text{Bi}_2\text{WO}_6$ sample. We elucidate that this shift may be attributed to the changes of the surrounding chemical environment of Bi and W after the introduction of Ag NPs. In Fig. 4c, the XPS spectrum of Ag displays two peaks at 374.2 and 368.1 eV, which are corresponding to Ag 3d_{5/2} and Ag 3d_{3/2}, respectively, of metallic Ag and rules out the existence of Ag₂O or others silver oxides in the sample [47,48]. The XPS spectrum of O1 s in $\text{WO}_3/\text{Bi}_2\text{WO}_6$ is presented in Fig. 4d and deconvoluted into three binding energy peaks at around 530.3, 531, and 532 eV, which are assigned to

Bi-O, W-O, and hydroxyl (O-H), respectively [49,50]. For the 2% Ag/ $\text{WO}_3/\text{Bi}_2\text{WO}_6$, the O1 s spectra are also deconvoluted into three peaks at 529.5, 530.3, and 531.2 eV. By comparing these obtained O 1 s peaks with that of the pristine Bi_2WO_6 and WO_3 in Fig. S3, it is found that the characteristic peaks of O 1 s shift to higher binding energy, ascribing to the formation of heterojunction in $\text{WO}_3/\text{Bi}_2\text{WO}_6$ hybrids, which results from the decrease of electron density around oxygen atoms because of WO_3 formation [51]. Furthermore, the peak intensity ratio of Bi-O to W-O significantly decreases by comparing the pristine Bi_2WO_6 and $\text{WO}_3/\text{Bi}_2\text{WO}_6$, which indicates that the compositional proportion of W-O increases. In contrast, when metallic Ag NPs are introduced, these characteristic peaks of O 1 s shift to lower binding energy, attributing to strong electron donor properties of the Ag NPs, which results in the increasing electron density around oxygen atoms. These findings demonstrate that the three-component heterojunction is successfully constructed by the facile one-pot hydrothermal and UV-assisted deposition route.

3.2. Optical properties and band structures of the obtained three-component heterojunctions

To investigate the photo-response range of the prepared samples, UV-vis diffuse reflection spectra were obtained and shown in Fig. 5. It is clearly observed that the light absorption ranges of Bi_2WO_6 , WO_3 , and $\text{WO}_3/\text{Bi}_2\text{WO}_6$ are located below 470 nm, which indicates that these samples could only take advantage of partial visible light and whole UV light. When Ag NPs are loaded on the surface of $\text{WO}_3/\text{Bi}_2\text{WO}_6$, the photo-response abilities of the Ag decorated hybrids to visible light are enhanced apparently due to the SPR effect of the metallic Ag NPs. Because the SPR effect stems from the collective oscillations of free electrons inside Ag NPs under certain photons irradiation, it could efficiently improve absorption ability of wide bandgap semiconductors to low energetic photons [52], resulting in an effective improvement of solar energy utilization during photocatalytic process. Although the peak intensity is low, which severely overlaps with absorption spectra

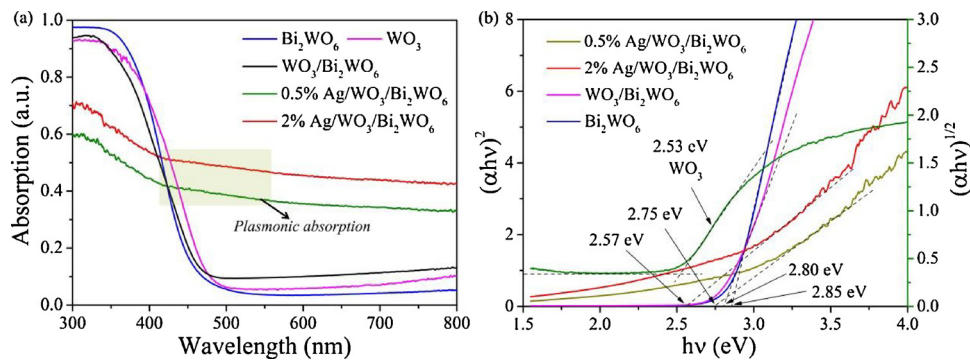


Fig. 5. (a) UV-vis diffused reflection spectra and (b) Tauc's plots of the prepared samples.

of Bi_2WO_6 and WO_3 , the plasmonic peak of Ag NPs can still be observed in the UV-vis absorption spectra in Fig. 5a and S5. The results demonstrated that the Ag NPs have been successfully deposited on the $\text{WO}_3/\text{Bi}_2\text{WO}_6$ heterojunction, which is agreement with the results of XRD and HRTEM.

Furthermore, the optical band gap energies of the as-prepared WO_3 , Bi_2WO_6 , $\text{WO}_3/\text{Bi}_2\text{WO}_6$ and Ag/ $\text{WO}_3/\text{Bi}_2\text{WO}_6$ samples were calculated from the UV-vis diffuse reflection spectra by the following equation near the band edge: $\alpha h\nu = A(h\nu - E_g)^{n/2}$, where α , ν , E_g , and A are absorption coefficient, light frequency, band gap and a constant, respectively [53]. The value of n is 1 or 4 for direct or indirect transition corresponding to Bi_2WO_6 and WO_3 , respectively. The band gaps of WO_3 , Bi_2WO_6 , $\text{WO}_3/\text{Bi}_2\text{WO}_6$, 0.5% Ag/ $\text{WO}_3/\text{Bi}_2\text{WO}_6$, 2% Ag/ $\text{WO}_3/\text{Bi}_2\text{WO}_6$ were calculated to be 2.53, 2.85, 2.80, 2.75 and 2.57 eV, respectively, as shown in Fig. 5b. It is concluded that the formation of WO_3 in one-pot synthesis of $\text{WO}_3/\text{Bi}_2\text{WO}_6$ leads to the bandgap decrease of Bi_2WO_6 from 2.85 to 2.80 eV. Moreover, the introduction of Ag NPs further reduces the apparent band gap of the hybrids from 2.80 to 2.57 eV in the three-component hybrids, displaying enhanced sunlight response ability. Furthermore, the low temperature EPR of the obtained samples exhibited that no signal attributed to the oxygen vacancy was detected, as shown in Fig. S4, which rules out that the oxygen vacancies are formed in the synthesized materials.

For further making clear the relative positions of the valence band (VB) and conduction band (CB) of the prepared samples, the total densities of the VB state spectra were taken, as shown in Fig. 6a. It is observed that the VB potentials of the pristine Bi_2WO_6 , WO_3 , and $\text{WO}_3/\text{Bi}_2\text{WO}_6$ samples are located at 2.19, 3.41, and 2.44 eV, respectively. The shift of the VB maximum potential of $\text{WO}_3/\text{Bi}_2\text{WO}_6$ to a more positive level demonstrates that the heterojunction between Bi_2WO_6 and WO_3 is successfully formed by the one-pot synthetic route. On the other hand, the VB maximum potential of 2% Ag/ $\text{WO}_3/\text{Bi}_2\text{WO}_6$ is located at 2.34 eV, higher than that of the $\text{WO}_3/\text{Bi}_2\text{WO}_6$. We suggest that this downshift is assigned to the introduction of metallic Ag acting as an

electron donor, resulting in more electrons to be filled in the VB and raising of the VB maximum level, as described in Fig. 6a. Finally, the apparent CB potentials of the prepared samples were calculated by means of the corresponding VB potential and the measured band gaps and the energy level distributions of CB and VB are summarized and illustrated in Fig. 6b. It is clearly observed that the bandgap of the Ag/ $\text{WO}_3/\text{Bi}_2\text{WO}_6$ hybrids is reduced, the potential of the top of VB shifts to the more positive potential, which can ensure enough potential of photoexcited holes to oxidize target reactants, such as organics and water.

3.3. Photocatalytic activity evaluation

The photocatalytic activities of the prepared samples for mineralization of gaseous halon-substituted VOCs, chlorobenzene, were measured under simulated sunlight irradiation. In Fig. 7a, conversion efficiencies of chlorobenzene on different photocatalysts are presented. It is found that only 7.8% of chlorobenzene is degraded in the absence of photocatalysts after 10 h irradiation. For the pristine Bi_2WO_6 and $\text{WO}_3/\text{Bi}_2\text{WO}_6$, the conversion efficiencies are 29% and 45%, respectively, which shows that the usage of photocatalysts apparently improve the photodegradation of chlorobenzene because of more reactive oxygen species releasing to oxidize chlorobenzene. The heterojunction between WO_3 and Bi_2WO_6 improves the photocatalytic activity in comparison with Bi_2WO_6 . In the case of Ag decorated $\text{WO}_3/\text{Bi}_2\text{WO}_6$ hybrids, the degradation efficiencies are remarkably enhanced to 70% and 80% on 0.5% Ag/ $\text{WO}_3/\text{Bi}_2\text{WO}_6$ and 2% Ag/ $\text{WO}_3/\text{Bi}_2\text{WO}_6$, respectively. The 2% Ag/ $\text{WO}_3/\text{Bi}_2\text{WO}_6$ hybrids display the best photocatalytic activity among the prepared samples, giving 1.8 and 2.8 times higher than the $\text{WO}_3/\text{Bi}_2\text{WO}_6$ heterojunction and pristine Bi_2WO_6 , respectively.

Furthermore, the kinetic rate constants were estimated to be 14.58, 11.42, 5.8, and 3.3 h^{-1} , corresponding to 2% Ag/ $\text{WO}_3/\text{Bi}_2\text{WO}_6$, 0.5% Ag/ $\text{WO}_3/\text{Bi}_2\text{WO}_6$, $\text{WO}_3/\text{Bi}_2\text{WO}_6$, and pristine Bi_2WO_6 , respectively, as

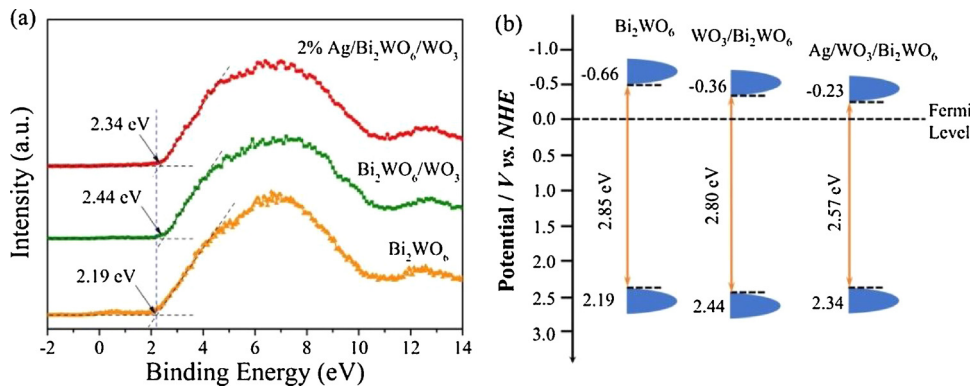


Fig. 6. VB XPS spectra (a) and energy level distributions of CB and VB (b) of the prepared Bi_2WO_6 , $\text{WO}_3/\text{Bi}_2\text{WO}_6$, and 2% Ag/ $\text{WO}_3/\text{Bi}_2\text{WO}_6$ samples.

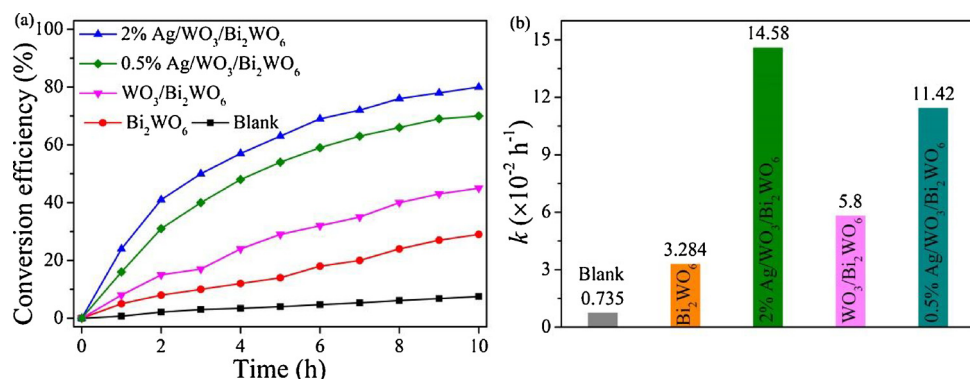


Fig. 7. Comparison of the photocatalytic activity (a) and the corresponding pseudo-first-order kinetic constants (b) of the as-prepared samples for the photocatalytic degradation of chlorobenzene under simulated sunlight irradiation.

presented in Fig. 7b. The activity data indicate that the decoration of metallic Ag nanoparticles allows more efficient reactive radicals to take part in the photodegradation of gaseous chlorobenzene under sunlight irradiation. It is concluded that the three-component Ag/WO₃/Bi₂WO₆ multi-junction could enhance the separation and utilization efficiency of photoinduced holes and electrons, leading to an improvement of the photocatalytic performance.

Moreover, real time monitoring of the photocatalytic process was evaluated by the *in-situ* FTIR (Fig. 8). After adsorption equilibrium of chlorobenzene on Ag/WO₃/Bi₂WO₆ in dark, the characteristic absorption peaks of chlorobenzene reached a stable level, and can be observed apparently. The strong bands at 3086 and 3038 cm⁻¹ are assigned to the C–H stretching vibrations of the aromatic ring in chlorobenzene and the bands at 1121, 1087, 1024 and 740 cm⁻¹ are attributed to the C–H out of plane vibration of the aromatic ring [54,55]. The bands at 1583, 1478, 1443, and 684 cm⁻¹ are resulted from the C=C skeleton vibration. In addition, the band at 712 cm⁻¹ belongs to the characteristic vibration of the Cl–C in chlorobenzene, and the other bands at about 2337 and 2360 cm⁻¹ are ascribed to C=O from CO₂ at ambient [56,57]. When the light was irradiated on the surface of the photocatalyst, the photogenerated holes would react with the adsorbed chlorobenzene molecules. It was observed that some characteristic bands change with the proceeding of photooxidation reaction. The bands at 3086 and 3038 cm⁻¹ are reduced significantly after 10 h irradiation, indicating that the aromatic ring is damaged efficiently. Meanwhile, it is found that the intensities of the bands relating to the aromatic ring, including C=C vibration and C–H out of plane vibration, decrease due to the ring-open and breakage of C–C. In contrast, the weak vibration peaks at

3850 and 3744, 2920 and 2850 cm⁻¹ corresponding to O–H stretching vibration of water and C–H stretching vibration of methyl [44,58], respectively, gradually increase, which further demonstrates that the aromatic ring has been attacked and broken efficiently by the photo-induced holes and formed hydroxyl radicals, resulting in production of chain intermediates. With the increasing reaction time, the bands at 1559 and 1540 cm⁻¹ ascribing to the asymmetric stretching vibration of COO⁻ groups and the bands at 1698 and 1716 cm⁻¹ reported as the stretching vibrations of C=O and C–O are continuously enhanced [59], accompanied with the increasing intensity of CO₂ features, which indicates that the short chain intermediates are further oxidized to aldehyde, carboxylic acids and finally mineralized to H₂O and CO₂.

3.4. Photocatalytic mechanism of the heterojunction composite

It is necessary to further explore the possible reaction mechanism that is beneficial for in-depth understanding the formation of multi-phase heterojunction and enhancement in the photocatalytic performance. In the previous reports, EPR has been demonstrated as a useful tool to probe the production of reactive oxygen species (ROS). For the 2% Ag/WO₃/Bi₂WO₆ heterojunction, the EPR data is presented in Fig. 9, in which both of hydroxyl radicals and superoxide radicals are captured in different conditions and detected, as described in experimental section. In Fig. 9a, the characteristic four peaks resulting from the DMPO–OH[·] are apparently observed, indicating that the photo-induced holes could react with the adsorbed H₂O and produce hydroxyl radicals [60]. On the other hand, when adjusting the media of reaction system from water to methanol, the DMPO indicator could efficiently

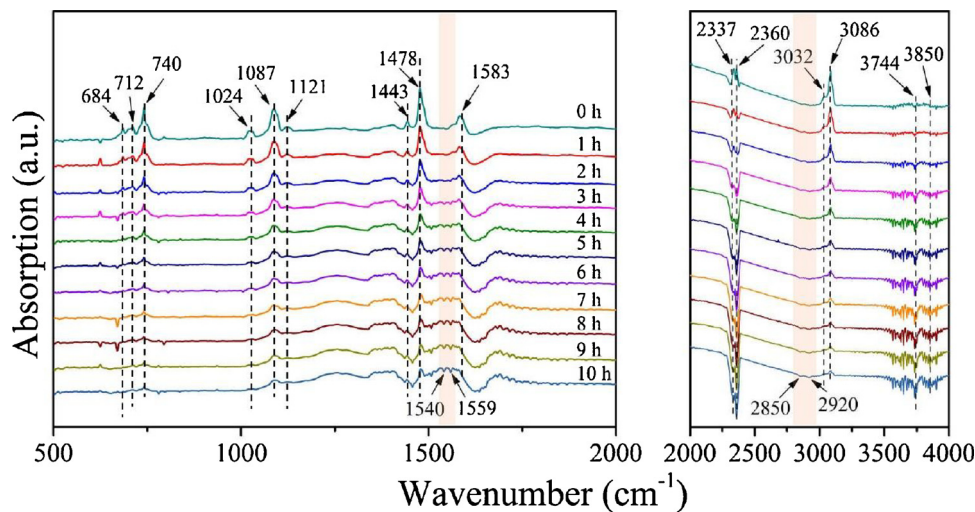


Fig. 8. *In situ* FTIR spectra of chlorobenzene photo-oxidation over the 2% Ag/WO₃/Bi₂WO₆ heterojunction under simulated sunlight irradiation.

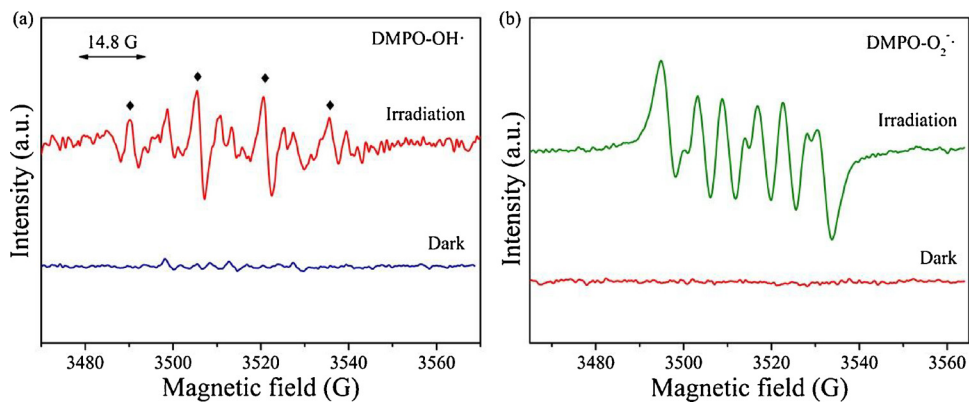


Fig. 9. EPR spectra of hydroxyl (a) and superoxide (b) radicals over the three-component 2% Ag/WO₃/Bi₂WO₆ heterojunction under simulated solar light irradiation.

capture the superoxide radicals (O₂^{·-}) and exhibit different signals from the hydroxyl radicals (·OH) [61]. As shown in Fig. 9b, it is clearly found that characteristic six peaks are detected under simulated solar light irradiation, which evidently demonstrates that the superoxide radical is also the ROS during the photocatalytic process. According to the above experimental data, it is confirmed that the photocatalytic activity of the pristine Bi₂WO₆ is improved after the formation of the multi-heterojunction among Ag NPs, WO₃, and Bi₂WO₆ in the Ag/WO₃/Bi₂WO₆ composites.

On the basis of characterization and activity evaluation data, band assignment and possible photocatalytic mechanism for the improved photocatalytic performance of Ag/WO₃/Bi₂WO₆ are described in Fig. 10. The CB and VB of Bi₂WO₆ are located at -0.66 and + 2.19 eV vs. NHE at pH = 0, respectively, and the CB and VB of WO₃ are situated at + 0.88 and + 3.41 eV, respectively. Therefore, Bi₂WO₆ and WO₃ could construct typical type-II heterojunction according to the band arrangement principle, as described in Fig. 10a. However, it is observed that the photoinduced electrons at the CB of Bi₂WO₆ will move to the VB of WO₃ due to the more positive potential of the CB of WO₃, which cannot react with the adsorbed oxygen to produce superoxide radicals. It is not in an agreement with the results of EPR where the superoxide radicals are demonstrated as the efficient ROS.

On the other hand, owing to the big difference of the CB between Bi₂WO₆ and WO₃, the Z-scheme structure could be used to explain the photocatalytic process, as presented in Fig. 10b. When the Ag/WO₃/Bi₂WO₆ heterojunction system is irradiated by simulated sunlight, the photogenerated electrons at the CB of WO₃ would rapidly quench with the photoinduced holes at the VB of Bi₂WO₆ inside the heterojunction

system. Meanwhile, the corresponding photoexcited electrons and holes still stay at the CB of Bi₂WO₆ and the VB of WO₃, respectively. Furthermore, owing to the existence of SPR effect, Ag NPs could be excited to produce free electrons, which could directly flow to the conduction band of WO₃ due to a lower Fermi level of Ag NPs (+ 0.14 eV vs. NHE) in comparison with WO₃ [62], thereby enhancing the surface electron excitation and interfacial electron transfer. As discussed above, the Z-scheme heterojunction realizes the efficient suppression of the recombination of photoinduced electron-hole pairs, which allows more photogenerated electrons and holes to participate in the reduction and oxidation reactions to form superoxide and hydroxyl radicals and finally mineralize chlorobenzene to small organics, CO₂, and H₂O.

4. Conclusion

Ag decorated Bi₂WO₆/WO₃ hybridized heterojunction with a Z-scheme band structure has been successfully synthesized for efficient removal of gaseous contaminants under simulated sunlight irradiation. The two-component WO₃/Bi₂WO₆ heterojunction was firstly fabricated based on the intercalation reaction between Bi ions and tungstate acid, which could efficiently form WO₃/Bi₂WO₆ Z-scheme heterostructure because of layer-by-layer crystal structure of WO₃ and Bi₂WO₆. Then Ag nanoparticles (NPs) were further introduced and uniformly anchored on the surface of WO₃/Bi₂WO₆, where the loaded Ag NPs could be beneficial for improving visible-light absorption and adjusting photoinduced charge carriers in the heterostructure through surface plasmon resonance (SPR). In comparison with the pure hierarchical Bi₂WO₆ and WO₃/Bi₂WO₆, the Ag/WO₃/Bi₂WO₆ heterojunction exhibits a better

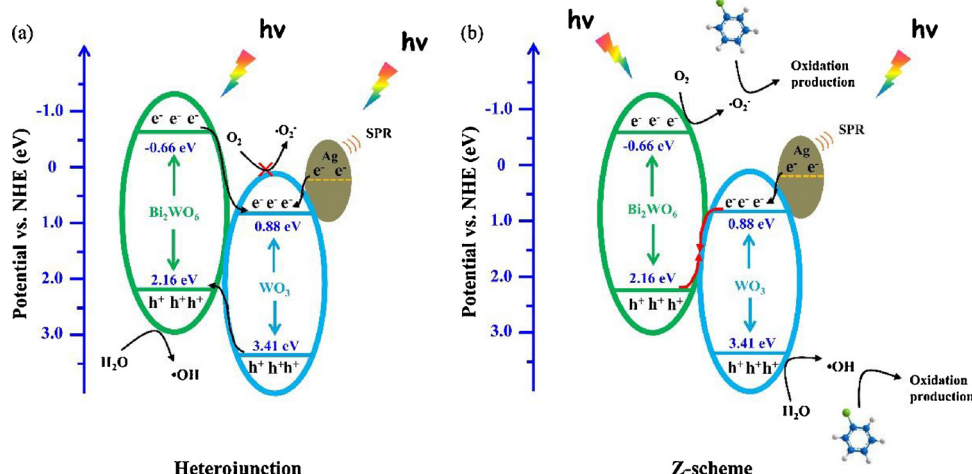


Fig. 10. Illustrator of different proposed photocatalytic mechanisms of Ag/WO₃/Bi₂WO₆ heterojunction: (a) the typical type-II heterojunction; (b) the Z-scheme structure.

photocatalytic activity for removal of gaseous chlorobenzene under simulated sunlight irradiation. The conversion efficiency of 2% Ag/WO₃/Bi₂WO₆ heterojunction is 2.5 and 1.9 times higher than that of the pristine Bi₂WO₆ and WO₃/Bi₂WO₆ samples. The improved photocatalytic activity is mainly attributed to the formation of three-component heterojunction and SPR of Ag NPs, which could not only increase the absorption of visible light, but also promote the separation efficiency of the photogenerated electrons and holes in the hybrids. It is found that the hydroxyl and superoxide radicals are the predominant ROS in the photocatalytic process deriving from reaction between photogenerated charge carriers and the adsorbed H₂O/O₂ molecules.

Acknowledgements

This work was financially supported by the National Natural Science Foundation of China (21501138), the Natural Science Foundation of Hubei Province (2015CFB177), and the Science Research Foundation of Wuhan Institute of Technology (K201513).

Appendix A. Supplementary data

Supplementary material related to this article can be found, in the online version, at doi:<https://doi.org/10.1016/j.apcatb.2018.09.090>.

References

- [1] A.L. Linsebigler, G. Lu, J.T. Yates, *Chem. Rev.* 95 (1995) 735–758.
- [2] H. Chen, C.E. Nanayakkara, V.H. Grassian, *Chem. Rev.* 112 (2012) 5919–5948.
- [3] S. Banerjee, S.C. Pillai, P. Falaras, K.E. Oshea, J.A. Byrne, D.D. Dionysiou, *J. Phys. Chem. Lett.* 5 (2014) 2543–2554.
- [4] J. Schneider, M. Matsuoka, M. Takeuchi, J. Zhang, Y. Horiuchi, M. Anpo, D.W. Bahneemann, *Chem. Rev.* 114 (2014) 9919–9986.
- [5] A. Iwase, S. Yoshino, T. Takayama, Y. Hau, Y.H. Ng, R. Amal, A. Kudo, *J. Am. Chem. Soc.* 138 (2016) 10260–10264.
- [6] A.H. Mamaghani, F. Haghigheh, C.S. Lee, *Appl. Catal. B: Environ.* 203 (2017) 247–269.
- [7] J. Qi, W. Zhang, R. Cao, *Adv. Energy Mater.* 8 (2018) 1701620.
- [8] L. Zhang, W.A. Anderson, S. Sawell, C. Moralejo, *Chemosphere* 68 (2007) 546–553.
- [9] Z. Cheng, Z. Gu, J. Chen, J. Yu, L. Zhou, *J. Environ. Sci.* 46 (2016) 203–213.
- [10] H.H. Huang, D.H. Tseng, L.C. Juang, J. Hazard. Mater. 156 (2008) 186–193.
- [11] N.K. Veldurthi, K.R. Eswar, S.A. Singh, G. Madras, *Catal. Sci. Technol.* 8 (2018) 1083–1093.
- [12] Y. Peng, Y. Zhang, F. Tian, J. Zhang, J. Yu, *Crit. Rev. Solid State* 42 (2017) 347–372.
- [13] J. Ke, X. Duan, S. Luo, H. Zhang, H. Sun, J. Liu, M.O. Tade, S. Wang, *Chem. Eng. J.* 313 (2017) 1447–1453.
- [14] D. Wang, P.S. Bassi, H. Qi, X. Zhao, L.H. Wong Gurudayal, R. Xu, T. Sritharan, Z. Chen, *Materials* 9 (2018) 348.
- [15] M.V. Lalić, Z.S. Popović, F.R. Vukajlović, *Comp. Mater. Sci.* 50 (2011) 1179–1186.
- [16] S. Sun, W. Wang, *RSC Adv.* 4 (2014) 47136–47152.
- [17] S. Luo, J. Ke, M. Yuan, Q. Zhang, P. Xie, L. Deng, S. Wang, *Appl. Catal. B: Environ.* 221 (2018) 215–222.
- [18] A. Rauf, M. Ming, S. Kim, M.S.A.S. Shah, C.H. Chung, J.H. Park, P.J. Yoo, *Nanoscale* 10 (2018) 3026–3036.
- [19] T. Saison, P. Gras, N. Chemin, C. Chaneac, O. Durupthy, V. Brezova, C. Colbeau-Justin, J. Jolivet, *J. Phys. Chem. C* 117 (2013) 22656–22666.
- [20] G. Dong, Y. Zhang, Y. Bi, *J. Mater. Chem. A Mater. Energy Sustain.* 5 (2017) 20594–20597.
- [21] X. Zou, Y. Dong, S. Li, J. Ke, Y. Cui, *Sol. Energy* 169 (2018) 392–400.
- [22] G. Cheng, M.S. Akhtar, O.B. Yang, F.J. Stadler, *J. Nanosci. Nanotechnol.* 16 (2016) 744–752.
- [23] W. Liu, L. Ling, Y. Wang, H. He, Y. He, H. Yu, H. Jiang, *Environ. Sci. Nano* 3 (2016) 745–753.
- [24] P. Dong, G. Hou, X. Xi, R. Shao, F. Dong, *Environ. Sci. Nano* 4 (2017) 539–557.
- [25] L. Jiang, X. Yuan, G. Zeng, J. Liang, X. Chen, H. Yu, H. Wang, Z. Wu, J. Zhang, T. Xiong, *Appl. Catal. B: Environ.* 227 (2018) 376–385.
- [26] J. Ke, H. Zhou, J. Liu, X. Duan, H. Zhang, S. Liu, S. Wang, *J. Colloid Interf. Sci.* 514 (2018) 576–583.
- [27] J. Low, C. Jiang, B. Cheng, S. Wageh, A.A. Al-Ghamdi, J. Yu, *Small Methods* 1 (2017) 1700080.
- [28] Q. Xu, L. Zhang, J. Yu, S. Wageh, A.A. Al-Ghamdi, M. Jaroniec, *Mater. Today* (2018), <https://doi.org/10.1016/j.mattod.2018.04.008>.
- [29] Y. Liu, H. Zhang, J. Ke, J. Zhang, W. Tian, X. Xu, X. Duan, H. Sun, M.O. Tade, S. Wang, *Appl. Catal. B: Environ.* 228 (2018) 64–74.
- [30] N. Wu, *Nanoscale* 10 (2018) 2679–2696.
- [31] M.J. Kale, T. Avanesian, P. Christopher, *ACS Catal.* 4 (2014) 116–128.
- [32] D. Chen, L. Gao, A. Yasumori, K. Kuroda, Y. Sugahara, *Small* 4 (2018) 1813–1822.
- [33] H. Huang, S. Wang, N. Tian, Y. Zhang, *RSC Adv.* 4 (2014) 5561–5567.
- [34] J. Ding, Q. Liu, Z. Zhang, X. Liu, J. Zhao, S. Cheng, B. Zong, W. Dai, *Appl. Catal. B: Environ.* 165 (2015) 511–518.
- [35] B. Ma, J. Guo, W. Dai, K. Fan, *Appl. Catal. B: Environ.* 123–124 (2012) 193–199.
- [36] H. Ma, J. Shen, M. Shi, X. Lu, Z. Li, Y. Long, N. Li, M. Ye, *Appl. Catal. B: Environ.* 121–122 (2012) 198–205.
- [37] W. Wang, M. Guo, D. Lu, W. Wang, Z. Fu, *Crystals* 6 (2016) 75.
- [38] Y. Li, J. Liu, X. Huang, J. Yu, *Dalton Trans.* 39 (2010) 3420–3425.
- [39] S.M.M. Zawawi, R. Yahya, A. Hassan, E. Mahmud, M.N. Daud, *Chem. Cent. J.* 7 (2013) 80.
- [40] M. Gui, W. Zhang, *J. Phys. Chem. Solids* 73 (2012) 1342–1349.
- [41] S. Sun, W. Wang, S. Zeng, M. Shang, L. Zhang, J. Hazad, *Mater.* 178 (2010) 427–433.
- [42] Y. Zhou, Z. Tian, Z. Zhao, Q. Liu, J. Kou, X. Chen, J. Gao, S. Yan, Z. Zou, *ACS Appl. Mater. Interfaces* 3 (2011) 3594–3601.
- [43] Y. Liang, S. Lin, L. Liu, J. Hu, W. Cui, *Appl. Catal. B: Environ.* 164 (2015) 192–203.
- [44] J. Liu, Y. Li, J. Ke, S. Wang, L. Wang, H. Xiao, *Appl. Catal. B: Environ.* 224 (2018) 705–714.
- [45] D. Jiang, W. Ma, P. Xiao, L. Shao, D. Li, M. Chen, *J. Colloid Interf. Sci.* 512 (2018) 693–700.
- [46] H. Khan, M.G. Rigamonti, G.S. Patience, D.C. Boffito, *Appl. Catal. B: Environ.* 226 (2018) 311–323.
- [47] J. Kang, Y. Sohn, *J. Mater. Sci.* 47 (2012) 824–832.
- [48] Y. Shi, D. Yang, Y. Li, J. Qu, Z. Yu, *Appl. Surf. Sci.* 426 (2017) 622–629.
- [49] Y. Peng, M. Yan, Q. Chen, C. Fan, H. Zhou, A. Xu, J. Mater. Chem. A Mater. Energy Sustain. 2 (2014) 8517–8524.
- [50] J. Liu, X. Li, R. Li, Q. Zhao, J. Ke, H. Xiao, L. Wang, S. Liu, M. Tade, S. Wang, *Appl. Catal. A Gen.* 549 (2018) 289–301.
- [51] Y. Su, B. Zhu, K. Guan, S. Gao, L. Lv, C. Du, L. Peng, L. Hou, X. Wang, *J. Phys. Chem. C* 116 (2012) 18508–18517.
- [52] I. Zada, W. Zhang, W. Zheng, Y. Zhu, Z. Zhang, J. Zhang, M. Imtiaz, W. Abbas, D. Zhang, *Sci. Rep.* 7 (2017) 17277.
- [53] J. Ke, J. Liu, H. Sun, H. Zhang, X. Duan, P. Liang, X. Li, M.O. Tade, S. Liu, S. Wang, *Appl. Catal. B: Environ.* 200 (2017) 47–55.
- [54] J. Wang, X. Wang, X. Liu, J. Zeng, Y. Guo, T. Zhu, *J. Mol. Catal. A-Chem.* 402 (2015) 1–9.
- [55] H. Huang, Y. Gu, J. Zhao, X. Wang, *J. Catal.* 326 (2015) 54–68.
- [56] J. Liu, Y. Li, Z.W. Li, J. Ke, H.N. Xiao, Y. Hou, *Catal. Today* 314 (2018) 2–9.
- [57] S. Albert, K. Keppler, P. Lerch, M. Quack, A. Wokaun, *J. Mol. Spectrosc.* 315 (2015) 92–101.
- [58] M. Mao, Y. Li, H. Lv, J. Hou, M. Zeng, L. Ren, H. Huang, X. Zhao, *Environ. Sci. Nano* 4 (2017) 373–384.
- [59] J. Sun, X. Li, Q. Zhao, J. Ke, D. Zhang, *J. Phys. Chem. C* 118 (2014) 10113–10121.
- [60] E. Grilla, A. Petala, Z. Frontistis, I.K. Konstantinou, D.I. Kondarides, D. Mantzavinos, *Appl. Catal. B: Environ.* 231 (2018) 73–81.
- [61] B. Liu, X. Li, Q. Zhao, J. Ke, M. Tade, S. Liu, *Appl. Catal. B: Environ.* 185 (2016) 1–10.
- [62] T. Schulmeyer, S.A. Paniagua, P.A. Veneman, S.C. Jones, P.J. Hotchkiss, A. Mudalige, J.E. Pemberton, S.R. Marder, N.R. Armstrong, *J. Mater. Chem.* 17 (2007) 4563–4570.